# Prediction of Fretting Crack Location and Orientation in a Single Crystal Nickel Alloy

J. F. Matlik [a,1], T. N. Farris [b], J. Haynes [c], G. R. Swanson [d], and G. Ham-Battista [e]

[a] *Rolls Royce Corporation, Box 420, Indianapolis, IN, 46206-0420, USA*

[b] *School of Aeronautics and Astronautics, Purdue University, 315 North Grant Street, West Lafayette, IN, 47907-2023, USA*

[c] *United Technologies Corporation, Pratt and Whitney Space Propulsion, 17900 Beeline Hwy, Jupiter, FL 33478*

[d] *EM20, Damage Tolerance Assessment Branch, NASA, Marshall Space Flight Center, AL 35812*

[e] *Sverdrup Technology, Inc., MSFC Group, 6703 Odyssey Drive, Suite 303, Huntsville, AL 35806*

## Abstract

Fretting is a structural damage mechanism arising between two nominally clamped surfaces subjected to an oscillatory loading. A critical location for fretting induced damage has been identified at the blade/disk and blade/damper interfaces of gas turbine engine turbomachinery and space propulsion components. The high-temperature, high-frequency loading environment seen by these components lead to severe stress gradients at the edge-of-contact that could potentially foster crack growth leading to component failure. These contact stresses drive crack nucleation in fretting and are very sensitive to the geometry of the contacting bodies, the contact loads, materials, temperature, and contact surface tribology (friction). Recently, a high-frequency, high-temperature load frame has been designed for experimentally investigating fretting damage of single crystal nickel materials employed in aircraft and spacecraft turbomachinery. A modeling method for characterizing the fretting stresses of the spherical fretting contact stress behavior in this experiment is developed and described. The calculated fretting stresses for a series of experiments are then correlated to the observed fretting damage. Results show that knowledge of the normal stresses and resolved shear stresses on each crystal plane can aid in predicting crack locations and orientations.

*Key words:* fretting, fretting fatigue, single crystal, contact

---

[1] This work was carried out at Purdue University. Funding was provided in part by

Fretting is a structural damage mechanism arising from a combination of wear, corrosion, and fatigue between two nominally clamped surfaces subjected to an oscillatory loading. Although this phenomenon plagues machinery of many kinds, the focus of this work is on critical aerospace components and materials that are continually driven to the limit of their load capacities for light weight design. Vibrations inherent to engine operation, high-frequency blade response due to unsteady aeroelastic drivers, and elevated temperatures aggravate fretting at the blade/disk and blade/damper interface of such high performance turbomachinery components. As a result, fretting in these components has become a focus of current research [1,2].

Despite the complexity of the fretting problem, there has been some success in predicting the fretting fatigue life using mechanics or stress based models. These models are formulated from information about the contact pressure, external load (or bulk load), coefficient of friction, and tangential load (or relative slip). The fact that these models show success for a variety of testing conditions suggests that some parameters may have *secondary* effects that could collapse into or be a part of the effects of a smaller set of *primary* variables [3]. A well defined, well characterized experimental setup in fretting could then be defined as one that allows characterization of these primary variables. In response to a recent need to investigate fretting behavior of turbine engine components under engine type loading and temperatures, a high-frequency, high-temperature fretting rig capable of investigating fretting behavior of advanced alloys has been constructed [4]. The remainder of this work serves to present the model developments used in analyzing the spherical, dissimilar, anisotropic material contact tests performed on this designed rig [5].

## 1 Mechanics of Fretting

In plain fatigue research, study of the component damage due to fatigue is generally broken up into three phases: (1) a crack initiation phase, (2) a period of early or short crack growth, (3) and finally a long crack propagation phase that is generally characterized by a Paris-type equation. In fretting, a condition of partial slip defined by slip (relative motion) and stick (no relative motion) near the contact interface develops. Per St Venant's principle, the stress state remote from the contact will be affected only slightly. As a result, the stick/slip interfacial mechanics result in a near-surface, multi-axial state of stress with severe stress gradients that significantly influence crack initiation

---

a National Science Foundation fellowship for J. F. Matlik and in part by Pratt and Whitney Space Propulsion under subcontract with the National Aeronautics and Space Administration (NASA) managed by Greg Swanson of the Marshall Space Flight Center (MSFC).

and early crack growth. It is in the early stages of crack formation and growth behavior that fretting fatigue is distinguished from plain fatigue. Once the crack grows beyond the influence of the contact stresses, crack growth can be modeled with plain fatigue methods. Conversely, by removing the bulk stress and looking purely at stresses arising from contact, it is possible to investigate the nucleation and early stages of crack development due to fretting (or contact fatigue) alone. Mechanics based models of fretting contact involve solving the frictional contact problem rigorously and as a function of time. A full solution of these problems involves attaining the relative displacement (stick/slip distribution) at the contact with a subsequent solution of the near-surface stress and strain fields which drive fretting crack formation. To find a link between the cyclic contact stresses, strains and fretting crack nucleation, it is necessary to first address this frictional contact problem for the case being investigated; hence, emphasis here will be given to three-dimensional, dissimilar, anisotropic material contact model developments. For the interested reader, an excellent review of fretting fatigue historically was provided by Waterhouse [6] with further details about the underlying mechanics of fretting fatigue having been reviewed by Szolwinski and Farris [7] and Hills and Nowell [8]. Further information about fretting and its affect on the structural integrity of in service components have been reviewed by Farris et al. [9].

## 2 Finite Element Modeling

Despite recent progress cited in the literature above, the limitations in generality of these solutions have pragmatically required the use of numerical solution procedures like the finite element method (FEM) or boundary element method (BEM) when solving three-dimensional, dissimilar, anisotropic contact problems. Although computational power continues to increase at record pace, any stress analyst employing a finite element (FE) code for contact stress solutions must be cognizant of the extremely fine mesh required for resolving edge-of-contact stress peaks and stress gradients associated with fretting. The computational demand and convergence difficulties increase further when solving three-dimensional problems. It therefore becomes important to identify the FE mesh resolution required to capture the edge-of-contact stresses that drive fretting crack nucleation. This necessarily requires comparison of simplified FE model results with analytical results to investigate the required degree of mesh resolution.

Recent investigations have exploited a FE method called submodeling to alleviate the computational expense associated with solving a frictional contact problem of an entire in-service structural component [10]. In submodeling, a smaller, adequately refined mesh (submodel) local to the contact can be used to get converged stresses in the area of interest by applying displacement boundary conditions interpolated from a larger global model of the contacting component. The submodeling process as applied to the frictional contact problem in dovetail attachments of turbomachinery has recently been investigated for two- [11] and three-dimensions [12]. This method exploits the fact that stresses and displacements away from the edge-of-contact region converge much more quickly.

The current modeling efforts employ this submodeling technique for a spherical contact geometry. In this process, a global (coarse) model of the fretting pad and specimen capable of modeling the experimentally generated load and boundary conditions is first constructed. The global model mesh is refined until displacement convergence occurs at the boundary location of the smaller submodel to be analyzed. The convergence criterion employed assumes convergence when all the nodes at the submodel boundary for the fine global model had converged displacements to within specified percentage of the displacement value found for the coarse global model solution.

A similar, isotropic material contact was chosen to investigate the ability of the submodeling approach to capture the contact tractions for the three-dimensional Mindlin problem. Comparison of the FE results with a simplified theoretical result will also give insight into the level of mesh refinement required for capturing the edge-of-contact stress peaks and sharp stress gradients inherent to the fretting problem. Each of the FE global and submodels employed were generated in I-DEAS, a commercially available CAD/CAM/CAE software, and were solved in ABAQUS, a commercially available FE package, each released to Purdue University on an academic license.

## *2.1 Global Model*

Figure 1 shows the global FE model geometry, loads, and constraints used in numerically solving the three-dimensional contact problem. The upper spherical indentor represents the contact pad which contacts the lower specimen model at a flat contact interface. The boundary conditions chosen for analysis of the Mindlin loading case required specifying vertical and horizontal constraints to prevent rigid body rotation or translation of the pad (see Figure 1). To best represent the behavior of the infinite half-space assumed in the Mindlin loading condition, a surrounding set of three-dimensional infinite elements were added around an appropriately fine hemisphere of finite elements comprising the specimen model. A very light set of springs in each translational direction was also included in both the pad and specimen models to ensure nonsingular matrices when applying the initial loading step. To investigate the partial slip and corresponding shear traction generated at the contact surface due to Mindlin loading, the global model was first subjected

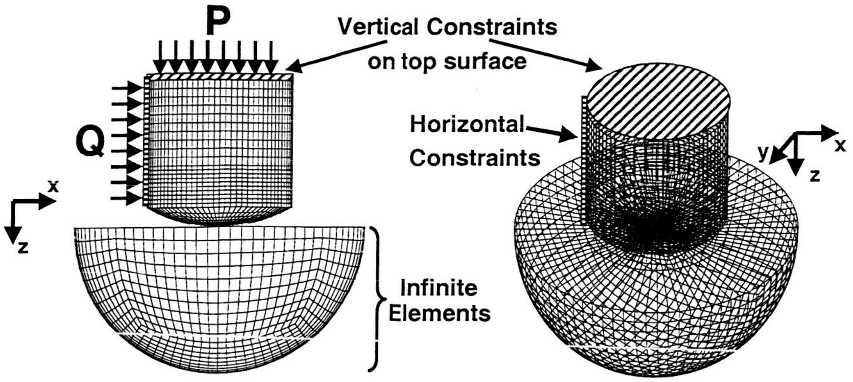

Fig. 1. A figure showing the global finite element model with appropriately applied loads and constraints for solving the three-dimensional contact problem.

to a normal load, P, in step 1 followed by the tangential load, Q, in subsequent step 2.

### *2.2 Submodel Process*

If stresses are desired within one contact diameter from the edge-of-contact, the extent of the finest submodel is set by knowledge of the dimensions of the contact patch. Classical Hertzian theory can be used to estimate the contact patch diameter for a spherical contact. With the geometric size of the finest submodel and global model now defined, an appropriate number of intermediate submodels can be chosen to ensure convergence. Since the displacement boundary conditions for the submodel are interpolated from the converged results of the global model, interpolation errors can arise from an inadequately fine global model. This fact must be taken into account when choosing the number of subsequent submodels to employ in the analysis.

Figure 2 highlights the submodeling scheme employed for this analysis. As illustrated in panel 1 of Figure 2, the first step in the submodel process is to solve the global model subjected to the experimentally determined loads and boundary conditions. Increasingly fine global models must be constructed and solved until the nodes at the boundary of the submodel in panel 2 have achieved convergence by meeting the chosen convergence criteria. In this analysis, convergence was assumed to have occurred when the nodes on the submodel boundary had converged to within 2%. An intermediate submodel (panel 2) is then solved by applying the appropriately interpolated displacement boundary conditions as obtained from the converged global model results in panel 1. Again, increasingly fine intermediate models must be run with the same converged displacement boundary conditions until convergence is maintained at the boundary for the next submodel in panel 3. In general, this process is repeated until the final submodel geometry is reached. Note that two successive

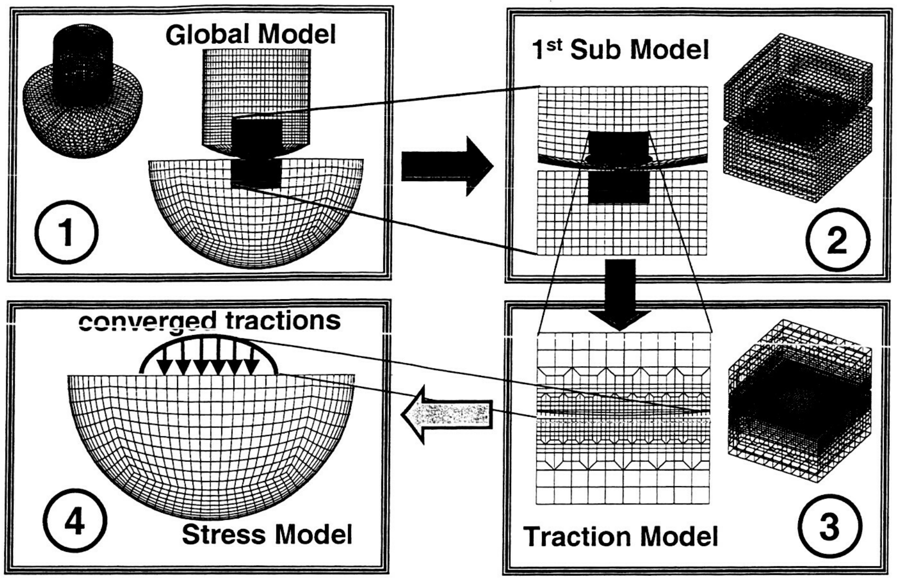

Fig. 2. Sequential depiction of the submodeling process to be employed in the three-dimensional contact analysis.

submodels (panel 2 and 3) were used to reach the final submodel extents.

Successively fine FE models for the traction model in panel 3 can now be run until convergence in tractions is obtained. Since a full solution of the nonlinear contact problem requires significant computational expense, the converged normal and shear tractions found from the traction model in panel 3 can then be appropriately interpolated and applied to a final stress submodel of the specimen for contact stress solution. Note that the final stress model (panel 4) is a hemisphere of elements where the spherical surface is subjected to fixed boundary conditions and the flat face is subjected to the converged tractions found from the traction model (panel 3). The radius of the hemisphere in the stress model was chosen to be large enough to adequately model a contact half space. To aid in stress convergence, the stress model (panel 4 in Figure 2) was built of quadratic brick elements instead of the linear brick elements used to obtain convergence in the previous submodels.

To appropriately apply tractions to the stress model, the converged contact tractions obtained by the traction model (panel 3 in Figure 2) first had to be interpolated to obtain traction values at corresponding nodes in the stress model (panel 4 in Figure 2). Details of the mesh geometry, loads, and boundary conditions of the stress model can be seen in Figure 3. After interpolating, the tractions at the nodes of the stress model need to be appropriately integrated and applied as equivalent nodal loads. Since the stress model was constructed of 20 noded quadratic brick elements, calculation of nodal loads requires appropriate integration of the tractions applied to the stress model contact surface comprised of 8 noded quadratic element surfaces. Successive solution of increasingly fine stress models were then performed until stress con-

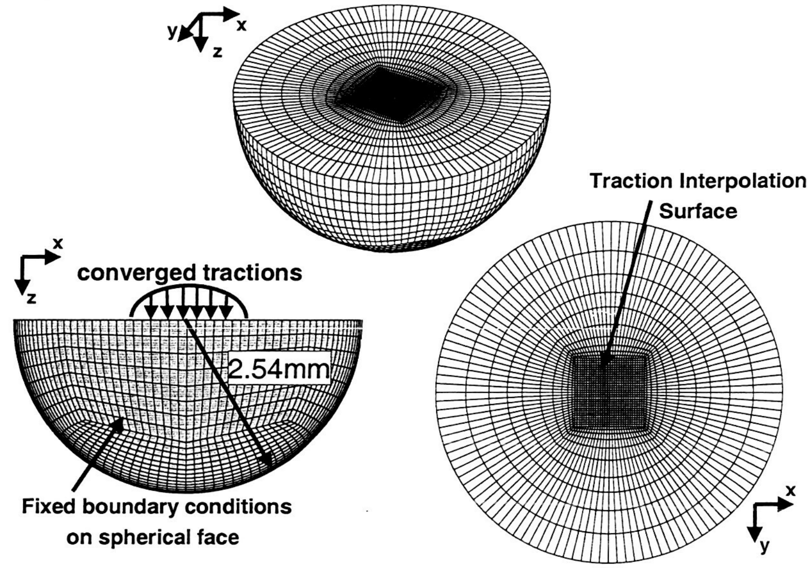

Fig. 3. Schematic of stress model mesh geometry, applied loads, and boundary conditions used in fretting subsurface calculation.

Table 1
Properties used in the similar material Mindlin loading example. Material properties are reflective of aluminum.

| Parameter | Value | Unit |
|---|---|---|
| Spherical Radius (R) | 6.35 (0.25) | mm (in) |
| Normal load ($P$) | 667 (150) | Newtons (lbs) |
| Tangential load ($Q$) | 89.0 (20) | Newtons (lbs) |
| Youngs Modulus (E) | 68.9 (10x$10^6$) | MPa (psi) |
| Poissons Ratio ($\nu$) | 0.33 | |

vergence for the region of interest is obtained. These converged stress results, when coupled with the experimentally observed loads and fretting damage development, can then be used to survey the ability of current fretting life prediction models to capture the fretting behavior of the contact problem of interest.

### *2.3 Similar Contact Example*

To investigate the mesh resolution required to obtain a converged traction solution, a similar, isotropic material contact analysis was first run. The global model geometry was defined with a spherical radius, R, and was subjected to a normal, P, and tangential load, Q, in the x-direction. Material properties reflective of an aircraft grade aluminum alloy (AL-2024) were used. A summary of the geometry, loading, and material properties used in this analysis can be seen in Table 1. A coefficient of friction, $\mu = 0.3$, was also assumed.

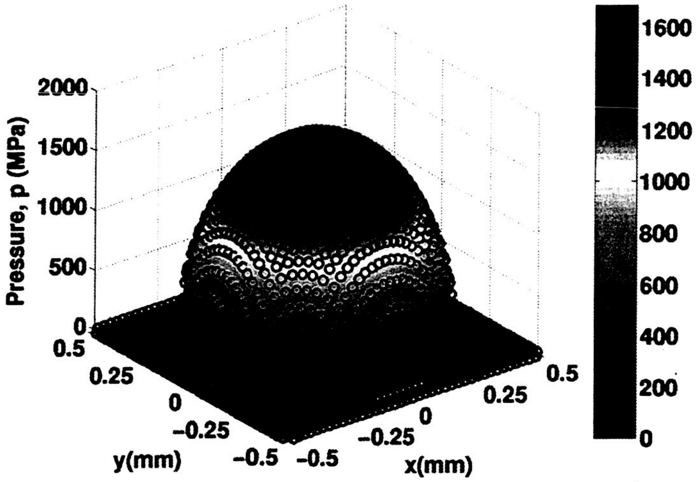

Fig. 4. Pressure traction solution as obtained from the FE submodeling process (circles) as compared with the Mindlin solution (contour surface).

The mesh resolution for each of the models were refined till the internal boundary location for the next submodel had converged displacements to less than

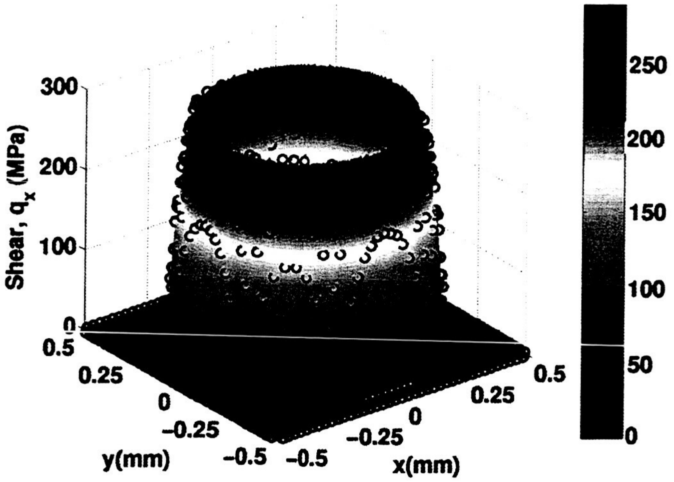

Fig. 5. Shear traction solution as obtained from the FE submodeling process (circles) as compared with the Mindlin solution (contour surface).

2%. The submodel process was employed and resulted in the normal and shear tractions as seen in Figures 4 and 5, respectively. In these contour plots, the circles represent the solution obtained from the submodel analysis and the surface plot represent the analytical solution as obtained from the axisymmetric Mindlin solution. Expressions for calculation of the Mindlin subsurface stress solution are presented in Hills, Nowell, and Sackfield (1993) .

It should also be noted that though the Mindlin solution represents a three-dimensional solution, it has been shown to only be exact on the plane of symmetry (y=0) for contacting materials exhibiting no Poisson's effect ($\nu = 0$) [14]. This Poisson's effect (Poisson's contraction) leads to out-of-plane shear tractions, $q_y$, that are not accounted for in the Mindlin solution which assumes that the shear traction only acts in the direction of the applied tangential load, Q. This effect is most exaggerated on a plane $\pm 45^o$ to the sliding direction for the case of incompressible bodies ($\nu = 0.5$). For comparison with the Mindlin solution, only the shear tractions, $q_x$, in the direction of the applied tangential load are reported.

To highlight the pressure and shear behavior, the pressure and shear traction solutions are plotted at planar slices x=0 (Figure 6) and y=0 (Figure 7). Note that the pressure and shear compare well to the analytical solution at x=0. However, the shear traction deviates from the analytical for the planar slice at y=0. Investigating this deviation from the Mindlin solution further reveals that the first step of loading, the application of the normal load, results in an axisymmetric slip and a resulting shear traction in the radial direction. This is reminiscent of the symmetric slip observed in two dimensional contact when a cylinder of one material is brought into contact with an infinite half-space of a different material [15]. Further investigation revealed that the Mindlin shear traction solution could be recovered by subtracting off the axisymmetric slip

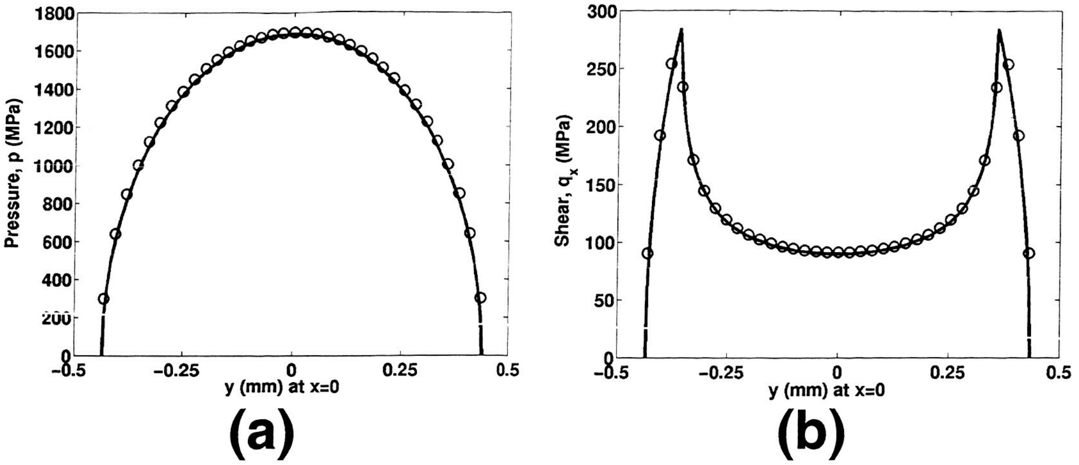

Fig. 6. A plot of (a) pressure, and (b) shear traction solutions for the x=0 planar location. Note the circles represent the numerical FEM result and the solid line represents the analytical Mindlin result.

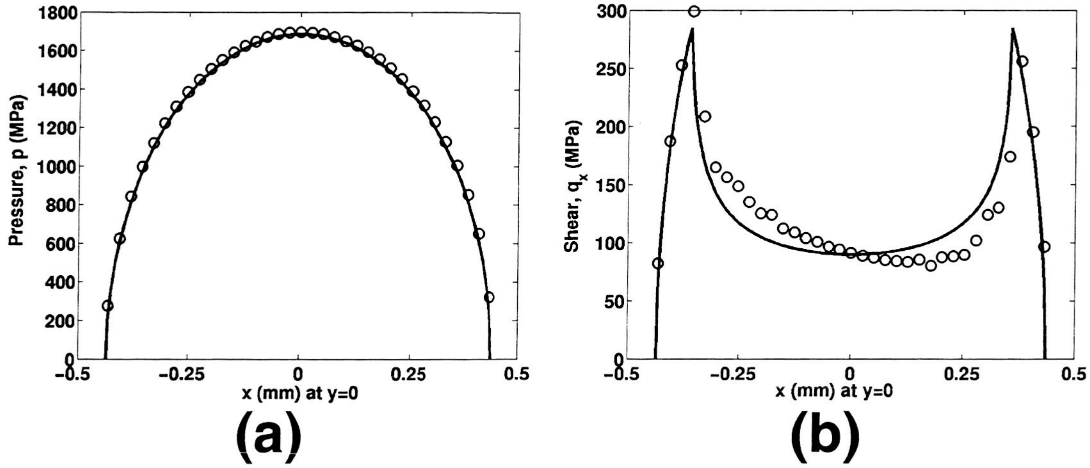

Fig. 7. A plot of (a) pressure, and (b) shear traction solutions for the y=0 planar location. Note the circles represent the numerical FEM result and the solid line represents the analytical Mindlin result.

developed in the first step of loading from the slip obtained in the second step of loading (see Figure 8). This effect is attributed to the fact that while the Mindlin solution assumes infinite half-spaces and infinite boundary conditions, finite element modeling requires that the boundary conditions and geometry of the pad be finite. This leads to the discrepancy between the submodel results and the theoretical results.

In order to appropriately apply the converged tractions to the stress model, the tractions as obtained at each nodal position in the traction submodel were interpolated to corresponding nodes in the stress model and then integrated to obtain equivalent nodal loads. These equivalent nodal loads were then applied to the corresponding contact nodes in the stress model. Using equation ??

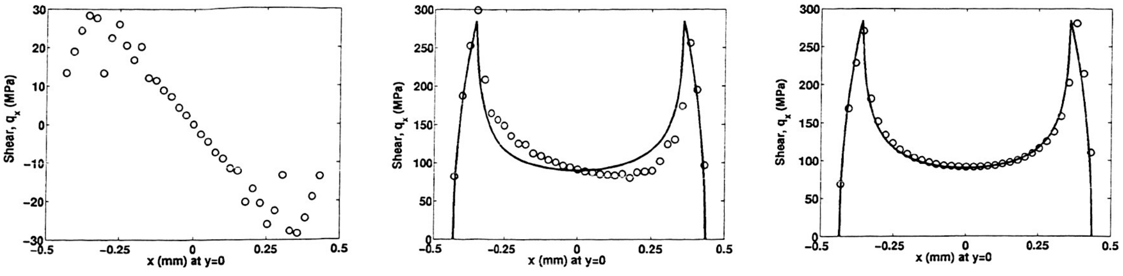

(a)

(b)

(c)

Fig. 8. Shear traction, $q_x$, developed at y=z=0 as found from the finite element solution for (a) the first step of loading (normal load only), and (b) the second step of loading (normal load and tangential load). Plot (c) shows that the Mindlin solution is recovered when the shear of the first step, (a), is subtracted from the shear of the second step, (b). Note the circles represent the numerical FEM result and the solid line represents the analytical Mindlin result.

and the method described previously, the calculated equivalent nodal loads for the similar material contact case were applied to the contact face of the stress model seen in Figure 3.

The converged tractions found from the traction model were applied to the stress model geometry with successively fine mesh resolutions. Figures 9,10,11,12,13, and 14 give the surface (z=0) stress solutions as obtained from the stress model solution. Note that each surface stress component as calculated by FEM

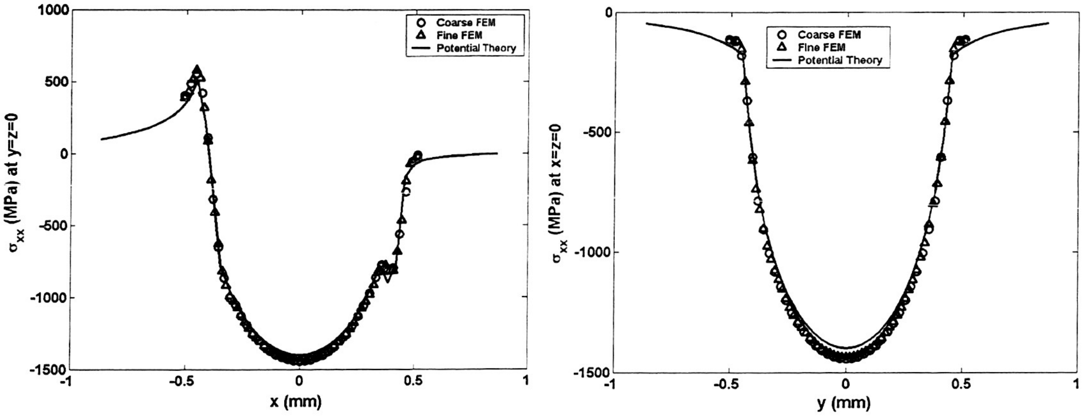

(a)

(b)

Fig. 9. A plot of subsurface stress $\sigma_{xx}$ at the surface (z=0) on the (a) x-axis (y=0), and (b) y-axis (x=0). Note the circles and triangles represent the numerical FEM results for the coarse and fine stress models, respectively. The solid line represents the analytical result.

matches the theoretical value well except for shear stress $\tau_{zx}$ at y=z=0 (Figure 13a) and shear stress $\tau_{yz}$ at x=z=0 (Figure 14b). These figures reflect difference in shear behavior observed in the converged shear tractions of the submodel analysis as illustrated in Figure 8. Hence, observing that the dif-

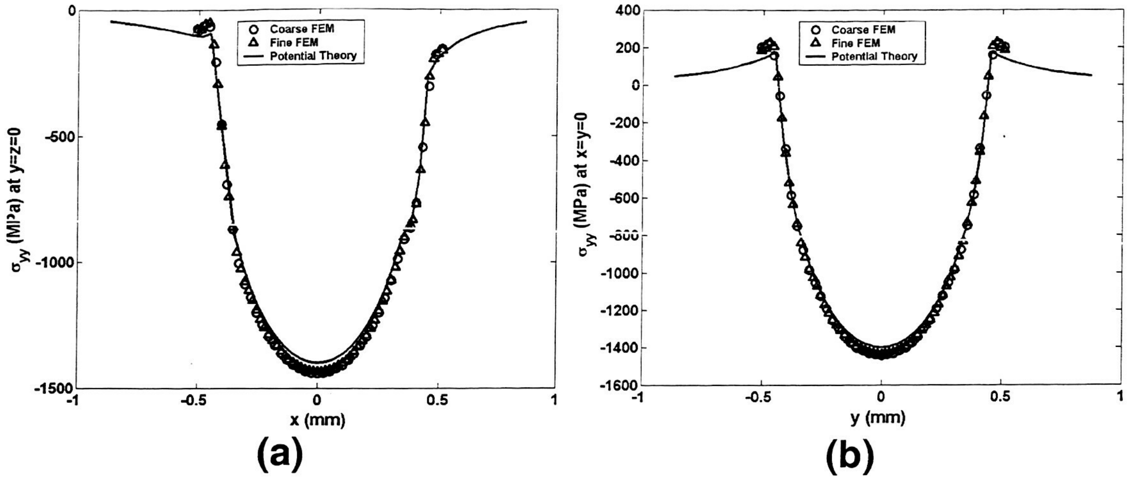

(a) (b)

Fig. 10. A plot of subsurface stress $\sigma_{yy}$ at the surface (z=0) on the (a) x-axis (y=0), and (b) y-axis (x=0). Note the circles and triangles represent the numerical FEM results for the coarse and fine stress models, respectively. The solid line represents the analytical result.

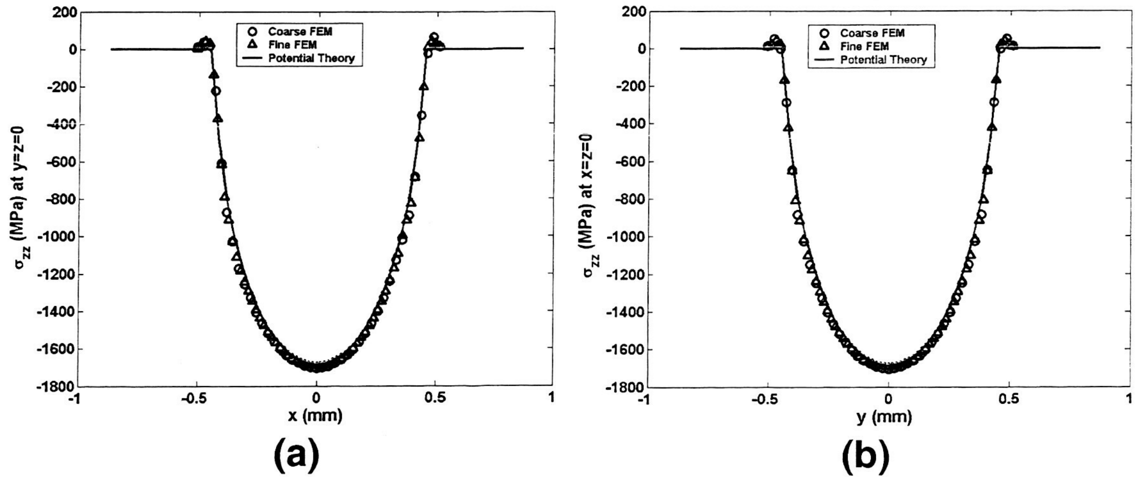

(a) (b)

Fig. 11. A plot of surface stress $\sigma_{zz}$ at the surface (z=0) on the (a) x-axis (y=0), and (b) y-axis (x=0). Note the circles and triangles represent the numerical FEM results for the coarse and fine stress models, respectively. The solid line represents the analytical result.

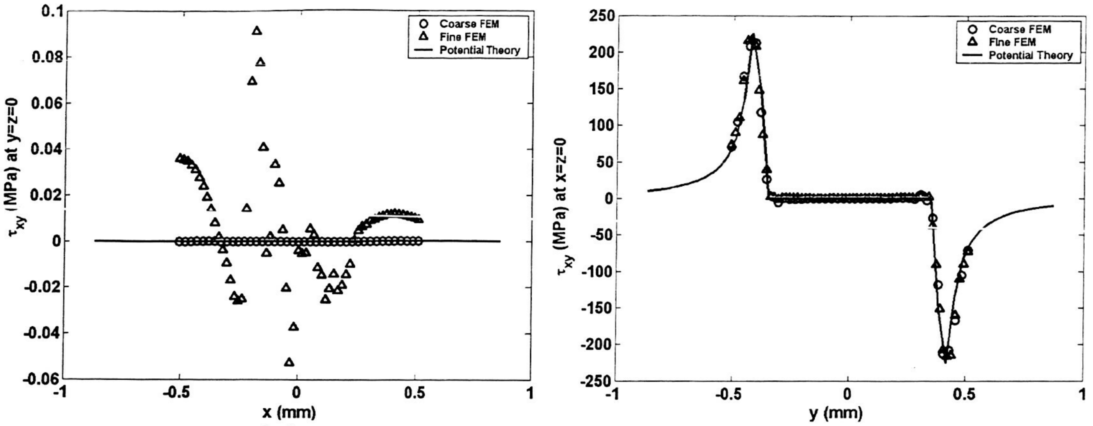

(a)

(b)

Fig. 12. A plot of subsurface shear stress $\tau_{xy}$ at the surface (z=0) on the (a) x-axis (y=0), and (b) y-axis (x=0). Note the circles and triangles represent the numerical FEM results for the coarse and fine stress models, respectively. The solid line represents the analytical result.

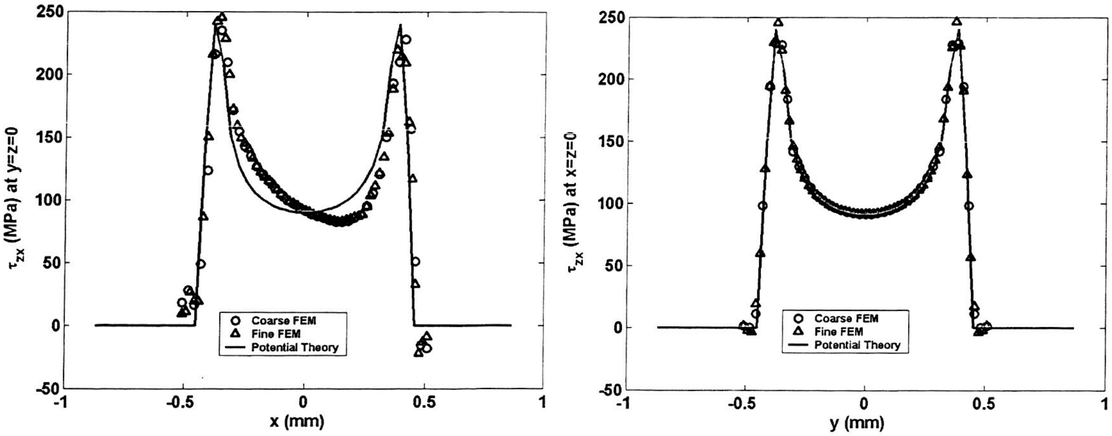

(a)

(b)

Fig. 13. A plot of surface shear stress $\tau_{zx}$ at the surface (z=0) on the (a) x-axis (y=0), and (b) y-axis (x=0). Note the circles and triangles represent the numerical FEM results for the coarse and fine stress models, respectively. The solid line represents the analytical result.

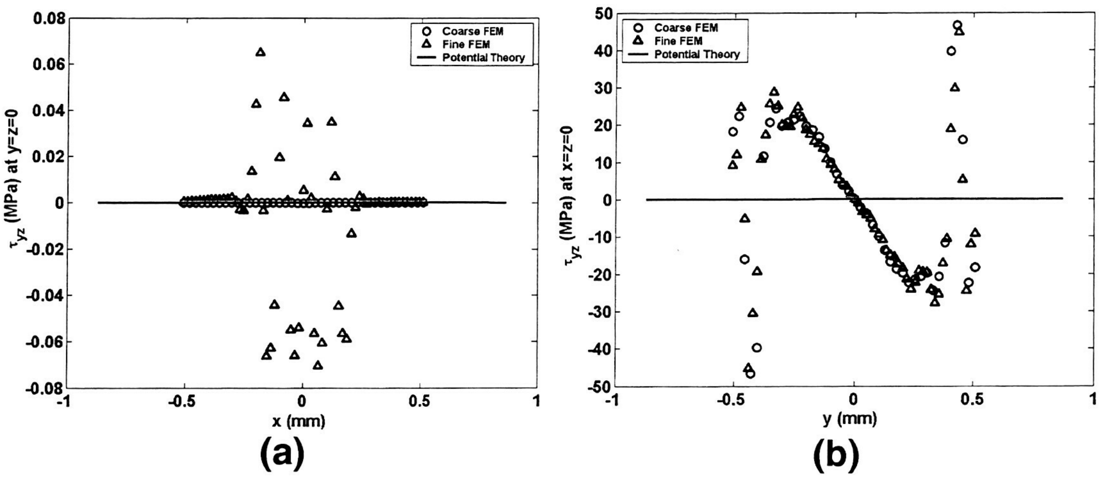

Fig. 14. A plot of subsurface shear stress $\tau_{yz}$ at the surface (z=0) on the (a) x-axis (y=0), and (b) y-axis (x=0). Note the circles and triangles represent the numerical FEM results for the coarse and fine stress models, respectively. The solid line represents the analytical result.

ference in shear behavior as compared to the Mindlin solution is a natural result of applying finite boundary conditions on the pad, the above result shows good agreement with potential theory. This suggests that the submodel / stress model solution procedure developed here can accurately predict shear tractions and near-surface stresses for the contact problem.

## 3 Extension to High-Temperature, Anisotropic Contact

The agreement of the similar contact solution presented provides confidence in ability of the submodeling approach to capture the tractions associated with three-dimensional contact. Extension of the similar contact submodeling approach to elevated temperature, dissimilar, anisotropic contact simply involves defining appropriate material properties for the pad and specimen FE models. Assuming that the experimental setup will maintain a relatively constant temperature through the duration of the experiment, material properties for the pad and specimen will be specified according to the chosen operational temperature. Since the pad is isotropic, standard isotropic material definition commands can be employed to define the constitutive relations. Defining the material properties for the specimen is more complicated due to the directional dependent constitutive behavior inherent to single crystal (anisotropic) materials. However, with careful attention to material orientation with respect to the global coordinate system, most finite element packages allow the user to implement general, anisotropic constitutive relations with previously defined subroutines. These subroutines calculate the appropriate elastic constants with knowledge of the crystal material principal axis orientation with respect to the global axes of the finite element.

## 4 Stress Analysis of Experiments

With knowledge of the in-situ fretting contact loads, the devised stress modeling technique can be employed to obtain the resulting fretting contact tractions and near-surface stresses.

### *4.1 Modeling the Experimental Contact*

Due to the finite dimensions of the test specimen and pad, it was necessary to construct a new global model capable of accounting for the finite specimen thickness. Figure 15 illustrates the mesh geometry, boundary conditions, and applied loads used for the global model of the experimental fretting contact. The pin geometry and boundary conditions are identical to those used in the similar material contact analysis. The full specimen geometry is accounted for in efforts to capture the finite boundary effects whose effects were demonstrated previously. To model the specimen as it is held in the specimen fixture, the back face and outer diameter of the specimen were subjected to fixed boundary conditions. In order to model the fretting contact test, the global model and subsequent submodeling were now subjected to three load steps:

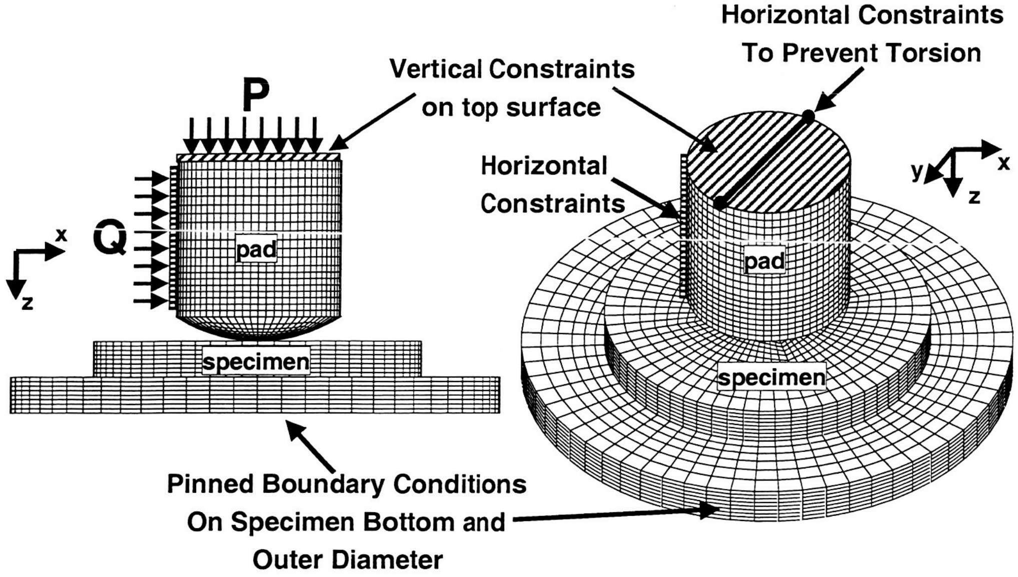

Fig. 15. Illustration of the global model mesh geometry, applied loads, and boundary conditions used to model the fretting experimental rig.

- LOAD STEP 1: Application of normal load, $P$, via a distributed pressure load on the top face of the contact pad.
- LOAD STEP 2: Application of maximum tangential load, $Q = Q_{max}$, via concentrated loads in the X-direction as seen in Figure 15.
- LOAD STEP 3: Application of minimum tangential load, $Q = Q_{min}$, via concentrated loads in the negative X-direction as seen in Figure 15.

The experiments displayed a near fully reversed tangential load ($Q_{min} = -Q_{max}$ or $R = -1$); therefore, the analysis performed here will assume this behavior. By ensuring displacement convergence on the submodel boundary, the global model of Figure 15 could then be employed in the submodeling method developed.

The material properties associated with the contact pad were characteristic of an isotropic polycrystalline material and the material properties associated with the contact specimen were characteristic of an anisotropic single crystal nickel (SNC) material. Table 2 gives a summary of the contact parameters

Table 2
Properties used in the analysis of the single crystal nickel / polycrystalline nickel contact tests. The material properties presented are representative of a common SCN and polycrystalline nickel alloy employed in aircraft engines.

| Parameter | Value | Unit |
|---|---|---|
| Spherical Radius (R) | 6.35 (0.25) | mm (in) |
| Specimen Thickness | 2.54 (0.1) | mm (in) |
| Normal load ($P$) | 445-578 (100-130) | Newtons (lbs) |
| Tangential load ($Q$) | $\pm 40$ to $\pm 89.0$($\pm 9$ *to* $\pm$ 20) | Newtons (lbs) |
| *Single Crystal Nickel Properties:* | | |
| Youngs Modulus ($E_{SX}$) | 108 (15.7) | GPa (MPa) |
| Poissons Ratio ($\nu_{SX}$) | 0.3995 | |
| Shear Modulus ($G_{SX}$) | 110 (15.9) | GPa (MPa) |
| *Inconel Material Properties:* | | |
| Youngs Modulus ($E$) | 183 (26.6) | GPa |
| Poissons Ratio ($\nu$) | 0.308 | |
| *Contact Properties:* | | |
| Coefficient of Friction ($\mu$) | 0.3 | |

used. These parameters reflect material properties of a common single crystal nickel alloy employed in aircraft engines used at greater than $600^o$C. The table also reports upper and lower bounds on the normal (P) and tangential (Q) loads as applied in the experiments. The cubic symmetry of SCN materials is characterized by three independent material constants which will be reported here with symbols $E_{SX}$, $\nu_{SX}$, and $G_{SX}$ where $G_{SX}$ is not a function of $E_{SX}$ and $\nu_{SX}$ as is the case with isotropic materials. Note that the reported normal and tangential loads in Table 2 are representative of but not exact loads applied in the experimental testing performed [5]. Using the given contact parameters, the developed submodel and stress model techniques can now be employed to solve for experimental contact stresses.

## *4.2 Crystal Plane Normal and Shear Stresses*

For a SCN material, the fatigue and fracture modes are highly dependent on the environmental conditions and stress state. The stress state is in turn greatly dependent on the applied loads and the crystal orientation with respect to those applied loads. Recently, a testing program to investigate fretting behavior of a SCN alloy took place in air at room temperature ($21^oC$ ($70^oF$)) and elevated temperature ($538^oC$ ($1000^oF$) and $649^oC$ ($1200^oF$)) representative of temperatures seen in gas turbine engine turbomachinery [5]. The material orientations were controlled for these tests and the contact loads were recorded from in-situ experimental monitoring.

SCN materials have a crystal structure that is face centered cubic (FCC). The high atomic density planes in an FCC crystal are the octahedral planes of which there are four. Each octahedral plane has six slip directions associated with them. Of the six slip directions on each plane, three are called *primary slip* (or easy slip) directions and three are called *secondary* slip directions. This results in a total of 24 slip directions (12 primary and 12 secondary slip directions) associated with the four octahedral planes [16]. In addition to the 24 octahedral slip directions, there are three cube planes, each of which have two slip directions per face. This gives a total of 30 slip directions comprised of 12 primary, 12 secondary and 6 cube slip directions on 4 octahedral and 3 cube planes.

With environmental conditions known, the obtained loads can now be used with the defined finite element submodel method to obtain experimental contact tractions and stresses. These stresses can then be used to solve the stress state for predicting fretting behavior of the SCN material. By converting the stresses obtained from the submodel analysis into the material coordinate system, it is possible to calculate the shear and normal stresses on each octahedral and cube plane using the appropriate kinematic equations. This stress behavior can then be related to the location of cracking identified from the experiments to provide insight into the active modes of crack growth in the specimen during fretting loading conditions. Further details describing the specific slip planes and slip directions in an FCC crystal can be found in Stouffer and Dame [16].

It has been observed that failure on the $\{111\}$ octahedral planes is governed by the behavior of the resolved shear stresses and not the maximum principal stresses [17]. However, the normal stress (mode I stress component) is thought to play a role in the failure process since the crack tip must remain open to allow fatigue and fracture to occur [18]. Based on these observations, the fretting damage observed in the experiments will be related to the calculated range of resolved shear stress in the 'i-th' slip direction, $\Delta\tau^i_{RSS}$, calculated as:

$$\Delta\tau^i_{RSS} = |\tau^i_{max} - \tau^i_{min}| \tag{1}$$

where $\tau^i_{max}$ is the resolved shear stress in the 'i-th' slip direction at the maximum applied tangential load, $Q_{max}$, and $\tau^i_{min}$ is the resolved shear stress in the 'i-th' slip direction at the minimum applied tangential load, $Q_{min}$. Since a crack will not propagate on a plane experiencing a compressive (crack closing) normal stress, the calculated resolved shear stress $\tau^i$ was set to zero if the normal stress of its corresponding crystal plane was compressive ($\sigma^i_n < 0$) at the location of stress calculation.

Although literature has commented that the crack driving force in SCN materials are the resolved shear stresses and not the crystal plane normal stresses [17], the normal stress range on each octahedral plane and cube plane can also be calculated for completeness. Therefore, the fretting damage is also compared to the normal stress range on the 'j-th' crystal plane, $\Delta\sigma_n^j$, calculated as:

$$\Delta\sigma_n^j = |\sigma_{nmax}^j - \sigma_{nmin}^j| \tag{2}$$

where $\sigma_{nmax}^j$ is the normal stress on the 'j-th' crystal plane at the maximum applied tangential load, $Q_{max}$, $\sigma_{nmin}^j$ is the normal stress on the 'j-th' crystal plane at the minimum applied tangential load, $Q_{min}$, and 'j' identifies one of the seven crystal planes of an FCC crystal. Again, since a crack will not propagate on a plane experiencing a compressive (crack closing) normal stress, the calculated normal stress ($\sigma_{nmax}^j$ or $\sigma_{nmin}^j$) was set to zero in equation 2 if the normal stress of its corresponding crystal plane was compressive ($\sigma_n^j < 0$) at the location of stress calculation.

## 5 Correlation of Crack Location and Orientation With Stresses

Defects or anomalies associated with intrinsic material quality (IMQ) serve as the source of fatigue crack initiations. The contribution and interplay of the operating environment, temperature, and stress condition strongly affect which defect species will be operative as well as the particular micromechanism by which the defect or IMQ initiates a fatigue crack. After initiation, the fatigue crack growth is dependent on the operative microscopic fracture mode [19]. Due to the complexity inherent to the two-phase microstructure of SCN materials, a complex set of fracture modes exist and are dependent on the environmental conditions, crystal orientation, temperature, and state of stress. To assist the relation of observed surface cracking behavior to the surface contact stresses, contours of the surface resolved shear stress ranges and associated crystal plane normal stress ranges on each slip plane were calculated using the devised submodel stress analysis.

### *5.1 Surface Contact Stresses*

To investigate the surface contact stress behavior as the material orientation was rotated, the submodel stress analysis was employed to observe locations of concentrated large resolved shear stress ranges and normal stress ranges for each slip plane at material orientations of $\Theta = 0^o, 15^o, 30^o$, and $45^o$. For each of the submodel analyses run, the normal load (P) was held constant at the target experimental value of 534 Newtons (120 lbs), the tangential load (Q) was held constant at 89 Newtons (20 lbs), and the coefficient of friction ($\mu$) was given a value of 0.3.

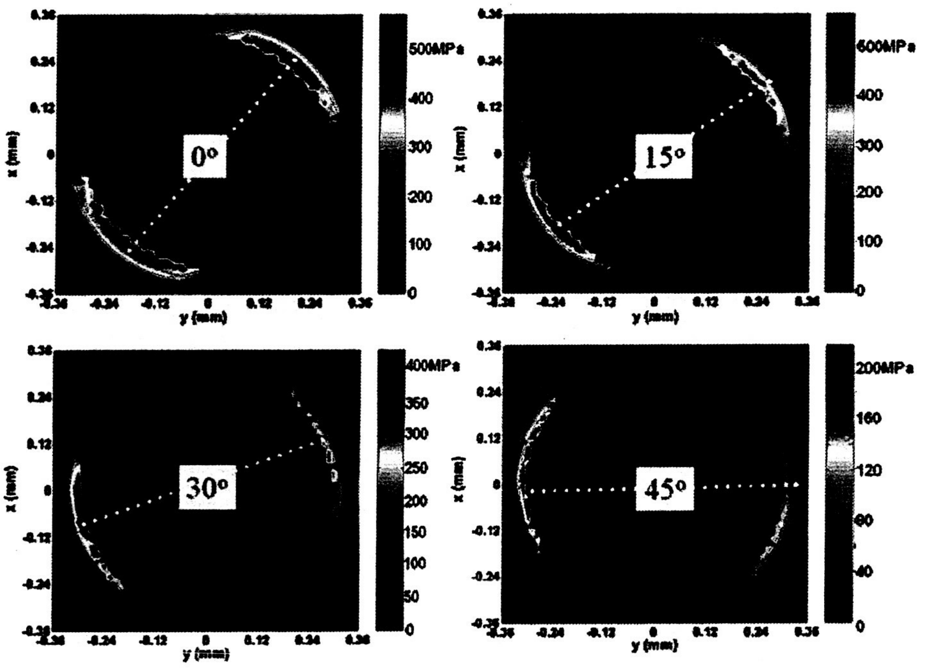

Fig. 16. Contour plots showing how the loci of large resolved shear stress ranges, $\Delta\tau^{6}_{RSS}$, for primary slip direction 6 in octahedral plane 2 rotates with material orientation. Note stresses reported are in MPa and the reported angle on each contour plot refers to the material orientation angle, $\Theta$.

### 5.1.1 *Resolved Shear Stress Range,* $\Delta\tau^{i}_{RSS}$

A representative surface contour plot of resolved shear stress range showing loci of large stress ranges for a particular slip plane can be seen in Figure 16. Observing this stress behavior with rotating material orientation reveals that the loci of concentrated large resolved shear stress ranges rotates with the material orientation. This is highlighted in Figure 16 by the white dotted lines that rotate with the material orientation and match the rotation of the loci of high resolved shear stress ranges.

Observing this behavior on each of the seven crystal planes in each slip direction revealed areas of large resolved shear stress range locations for each slip direction and were mapped to the slip annulus as seen in Figures 17 and 18. Figure 17 shows large resolved shear stress range loci for the four octahedral planes, and Figure 18 shows large resolved shear stress range loci for the cubic planes of the FCC single crystal nickel specimens. Note that in these pictures the location of large resolved shear stress locations for each slip plane rotate with the material orientation as observed previously.

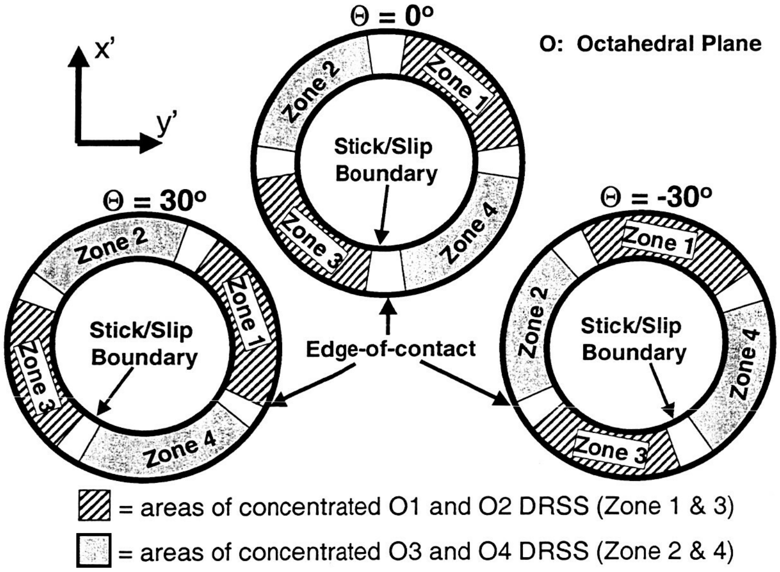

Fig. 17. Schematic highlighting the areas along the slip annulus where the concentration of large resolved shear stress ranges, $\Delta\tau^{i}_{RSS}$, exist for octahedral slip planes.

### 5.1.2 *Crystal Plane Normal Stress Range,* $\Delta\sigma^{j}_{n}$

A representative surface contour plot of the normal stress range for a crystal plane showing loci of large stress ranges can be seen in Figure 19. Similar to the resolved shear stress behavior, observing the normal stress behavior with rotating material orientation reveals that the loci of concentrated large normal stress ranges also rotates with the material orientation. This is highlighted in

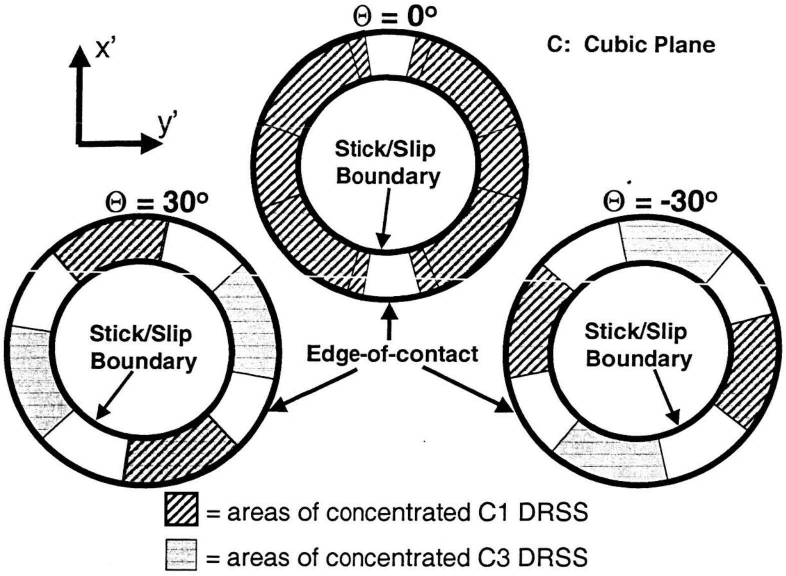

Fig. 18. Schematic highlighting the areas along the slip annulus where the concentration of large resolved shear stress ranges, $\Delta\tau^{i}_{RSS}$, exist for cubic slip planes.

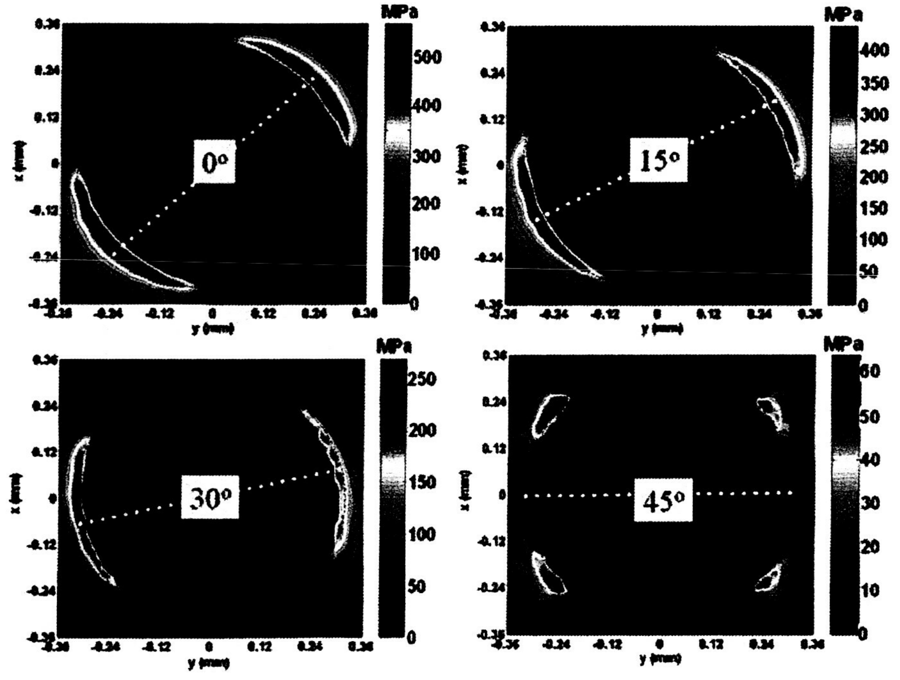

Fig. 19. Contour plots showing how the loci of large normal stress ranges, $\Delta\sigma_n^2$, for octahedral plane 2 rotates with material orientation. Note stresses reported are in MPa and the reported angle on each contour plot refers to the material orientation angle, $\Theta$.

Figure 19 where the white dotted lines rotate with the material orientation and match the rotation of the loci of high normal stress ranges.

Observing this behavior on each plane was used to identify areas of large normal stress range locations for each plane and were mapped to the slip annulus, similar to the resolved shear stress range case. The loci of large normal stress ranges for the octahedral planes behave the same as in Figure 17. However, the loci of large normal stress ranges for the cube plane differs as illustrated in Figure 20. Hence, Figure 17 shows large normal stress range loci for the four octahedral planes, and Figure 20 shows large normal stress range loci for the cubic planes of the FCC single crystal nickel specimens.

Note that the normal stress range values on cube plane 2 are negligible at the surface and therefore are not presented here.

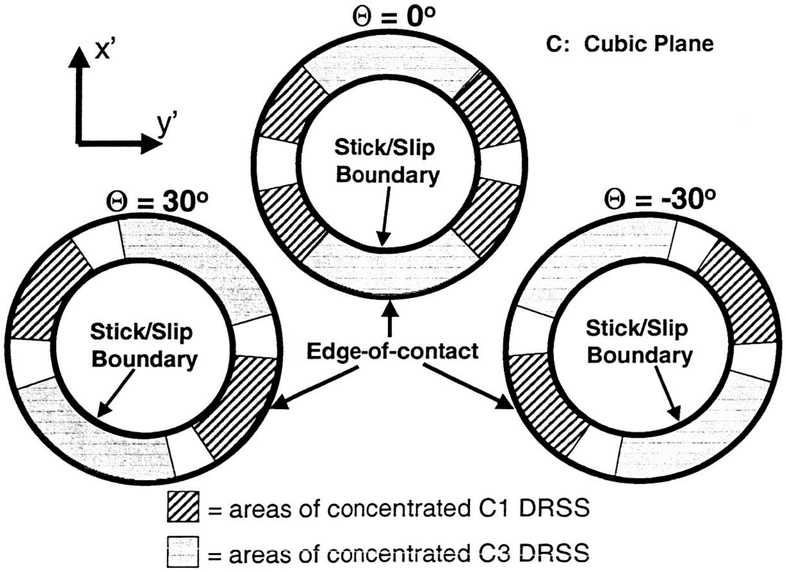

Fig. 20. Schematic highlighting the areas along the slip annulus where the concentration of large normal stress ranges, $\Delta\sigma_n^j$, exist for cubic slip planes.

### *5.2 Theoretical Crack Propagation Orientations*

For the case of crystallographic propagation, cracks will propagate along one of the crystal planes. Depending on the orientation of the material axes of the crystal, the crystal planes will be oriented at different angles with respect to the specimen surface. Figure 21 shows the crystal material axes orientation with respect to the specimen when the applied tangential load and x'-axis is oriented with one of the crystal axes ($\Theta = 0$). Figure 21 can then be used with the definitions of the 30 slip directions as defined by Stouffer and Dame ([16]) to determine the slip planes and directions with respect to the experimental

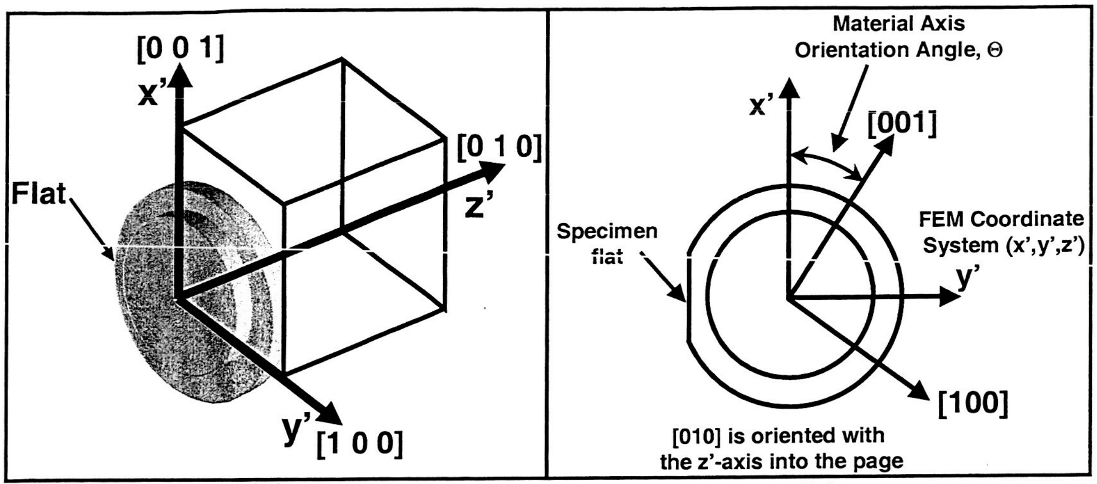

(a) (b)

Fig. 21. Schematic showing the crystal structure orientation with respect to the top hat specimen used in the high-frequency, high-temperature tests for case when the x'-axis is aligned with the [0 0 1] material axis and the y'-axis is aligned with the [1 0 0] material axis.

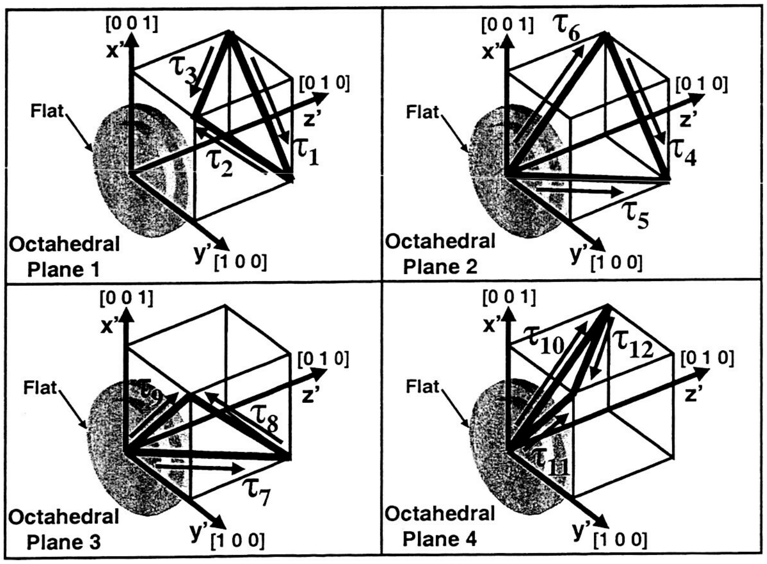

Fig. 22. Schematic showing primary slip direction orientations with respect to the top hat specimen used in the high-frequency, high-temperature tests for case when the x'-axis is aligned with the [0 0 1] material axis and the y'-axis is aligned with the [1 0 0] material axis.

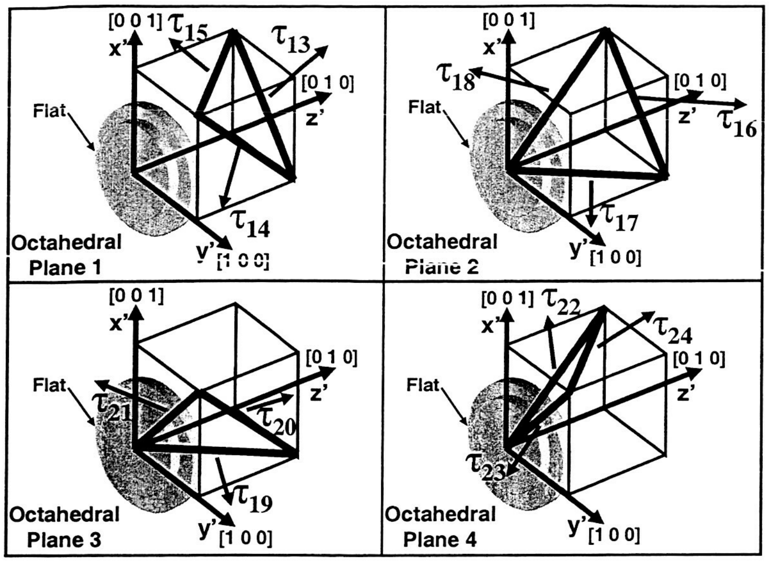

Fig. 23. Schematic showing secondary slip direction orientations with respect to the top hat specimen used in the high-frequency, high-temperature tests for case when the x'-axis is aligned with the [0 0 1] material axis and the y'-axis is aligned with the [1 0 0] material axis.

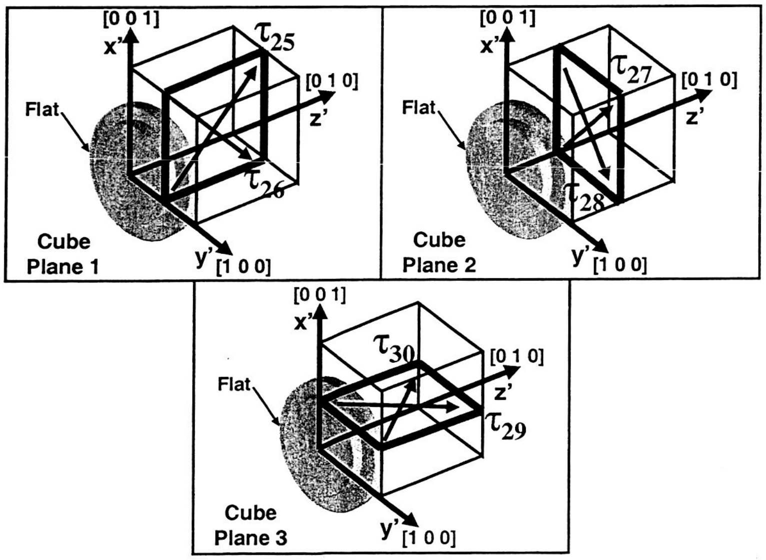

Fig. 24. Schematic showing cube slip direction orientations with respect to the top hat specimen used in the high-frequency, high-temperature tests for case when the x'-axis is aligned with the [0 0 1] material axis and the y'-axis is aligned with the [1 0 0] material axis.

specimens as seen in Figures 22, 23, and 24. The slip directions with respect to the specimen can then be found for any arbitrary material direction, $\Theta$, by rotating the slip directions as displayed in Figures 22, 23, and 24 an angle $\Theta$ about the z'-axis.

Theoretically for the crystal orientation in Figures 22, 23, and 24, crystallographic crack propagation would result in cracks oriented according to the directions displayed in Figure 25 for $\Theta=0^o$. Note that cracks propagating on octahedral planes 1 and 2 will theoretically be in the same orientation, and cracks propagating on octahedral planes 3 and 4 will theoretically be in the same direction and $90^o$ different than octahedral planes 1 and 2. These theoretical crack orientations also rotate with the material orientation as illustrated in Figure 25 for $\Theta = \pm 30^o$.

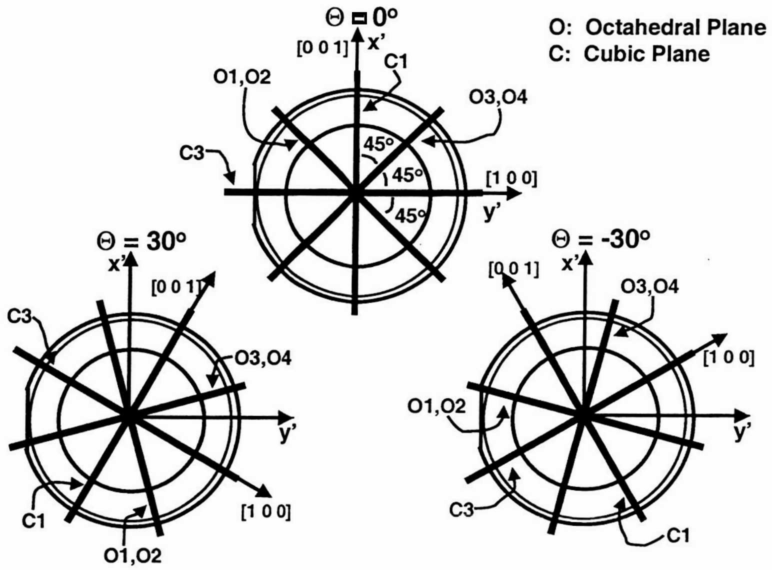

Fig. 25. Schematic showing theoretical surface crack orientations according to slip plane. The octahedral planes are identified with an 'O' for octahedral and the cubic planes are identified with a 'C' for cubic. The lines representing the plane orientations are radially spaced evenly at $45^o$.

Coupling knowledge about the peak resolved shear stress range loci with respect to the slip annulus as presented in Figures 17 and 18 with the theoretical crack propagation directions as displayed in Figure 25 result in predicted orientations for cracks that initiate at different locations along the annulus. Using these observations, the orientations of cracks observed in the experimental testing program can be predicted based on the observed location of the cracking. If the resolved shear stress range can be used as a valuable parameter in fretting contact design and analysis of single crystal nickel materials, then prediction of crystallographic crack propagation orientations should match with the active slip plane where it forms.

For example, consider Figure 26. The scanning electron microscope image at the far left of the figure is of the upper wear scar on specimen J3-001-06, a specimen with a material orientation of $\Theta = 0^o$. The boxes highlight the extent of cracking in the slip annulus and the direction of applied tangential load, Q, with respect to the SEM image is indicated. Relating the observed cracking at the upper right of the slip annulus ($\Omega = 45^o$) to the calculated surface resolved shear stress ranges reveals that the largest $\Delta\tau^i_{RSS}$ at that location occurs on octahedral plane 1 in slip direction 2 (i=2) as illustrated by the upper contour plot in Figure 26. This suggests that the crack will form and propagate along the first octahedral plane (plane 1 of Figure ??). Figure 25 can then be used to predict the expected crack orientation. The predicted crack propagation orientation and the actual crack orientation can be seen in the upper right SEM micrograph of Figure 26. Relating the observed cracking at the bottom left of the slip annulus ($\Omega = -135^o$) to the calculated surface resolved shear stress ranges reveals that the largest $\Delta\tau^i_{RSS}$ at that location occurs on octahedral plane 2 in slip direction 6 (i=6) illustrated by the lower contour plot in Figure 26. This suggests that the crack will form and propagate along the second octahedral plane. Figure 25 can then be used to predict the expected crack orientation. Again, the predicted crack propagation orientation and the actual crack orientation can be seen in the lower right SEM micrograph of Figure 26.

The same prediction scheme can be performed using information about the loci of normal stress ranges. Figure 27 shows that the normal stress ranges predict the same location and orientation behavior for the experimentally observed cracks as the resolved shear stress ranges predicted in Figure 26. It is important to note that the peak normal stress ranges suggest that cracking should occur at the edge of contact. However, the majority of the cracking behavior observed experimentally showed cracks to initiate and grow within the slip annulus as predicted by the resolved shear stress ranges. Figures 26 and 27 illustrate the process that was performed for each wear scar investigated. A comparison of the observed and predicted crack locations and orientations for each test are presented in Table 3.

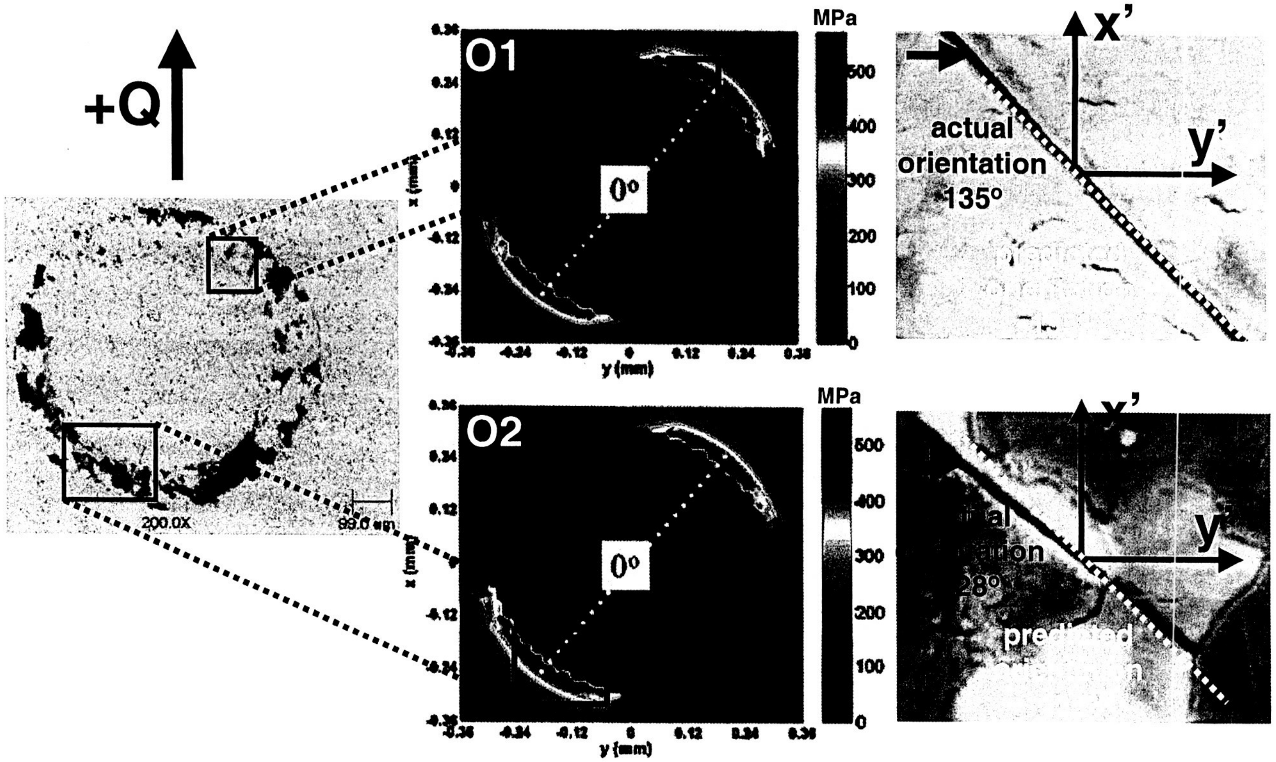

Fig. 26. Illustration of how crack orientations are predicted based on experimentally observed crack locations for a material orientation of $\Theta = 0^o$ and the behavior of the resolved shear stress ranges, $\Delta\tau^i_{RSS}$. Note that the surface contour plots of resolved shear stress ranges are reported in MPa.

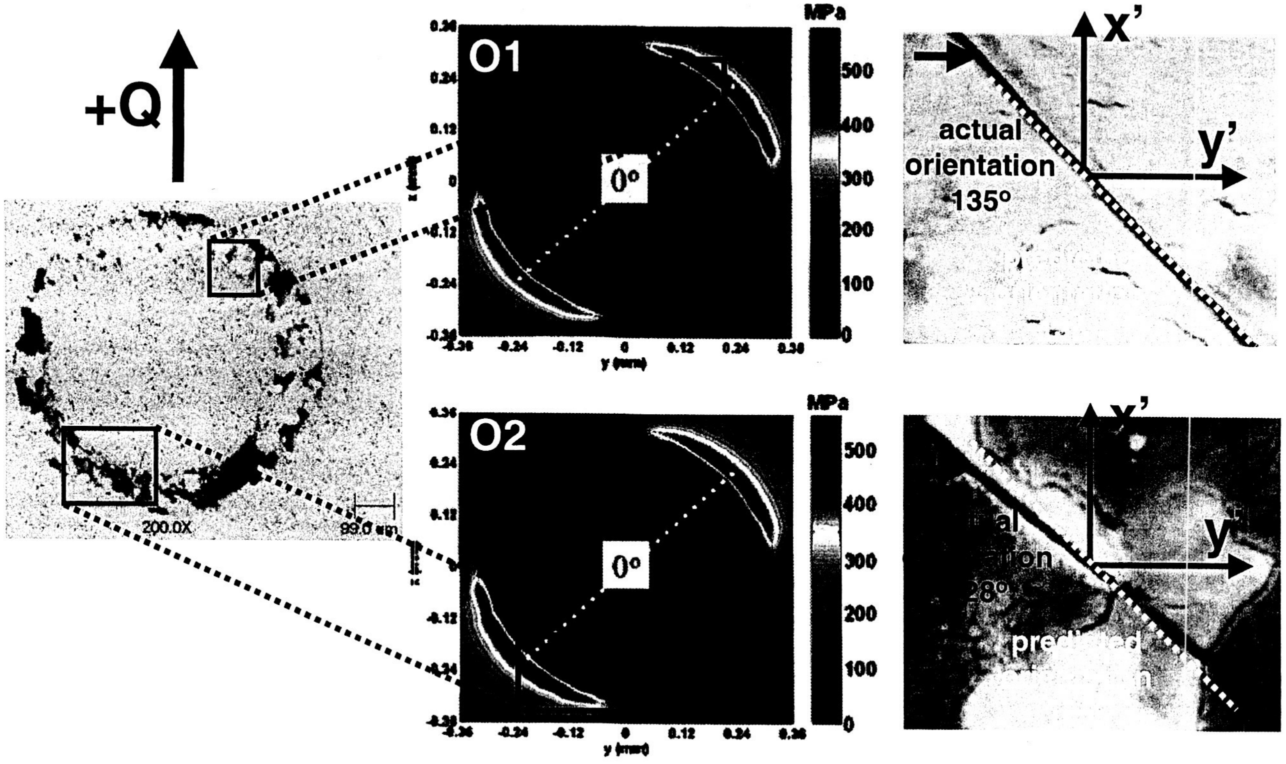

Fig. 27. Illustration of how crack orientations are predicted based on experimentally observed crack locations for a material orientation of $\Theta = 0^o$ and behavior of the normal stress ranges, $\Delta\sigma_n^j$. Note that the surface contour plots of resolved shear stress ranges are reported in MPa.

Table 3
Comparison of predicted and observed crystallographic crack locations and orientations for performed room-temperature high-frequency fretting tests. The propagation planes are identified with an 'O' for octahedral and a 'C' for cubic. Note that the material orientation of the high temperature specimens is unknown; therefore, no comments on crack propagation plane can be made without first identifying material orientation.

| Test ID. | Spec ID. | Observed Location $\Omega$(deg) | Actual Orientation $\Omega_c$(deg) | Actual Propagation Plane | Predicted Orientation $\Omega_c$(deg) | Predicted Propagation Plane |
|---|---|---|---|---|---|---|
| HFRT005 | J3-30D-01 | 0 | 101 | O1 or O2 | 105 | O1 or O2 |
| | J3-30D-02 | 90 | 80 | O3 or O4 | 165 | O1 or O2 |
| | | 180 | 77 to 83 | O3 or O4 | 75 | O3 or O4 |
| HFRT006 | J3-30D-02 | -105 | 165 to 172 | O1 or O2 | 165 | O1 or O2 |
| | | 90 | 172 | O1 or O2 | 165 | O1 or O2 |
| | | 180 | 84 to 85 | O3 or O4 | 75 | O3 or O4 |
| HFRT007 | J3-30D-01 | 180 | 100 to 102 | O1 or O2 | 105 | O1 or O2 |
| | J3-30D-02 | -90 | 168 to 171 | O1 or O2 | 165 | O1 or O2 |
| HFRT008 | J3-30D-03 | 180 | 75 | O3 or O4 | 75 | O3 or O4 |
| | J3-30D-04 | -90 | 145 | C1 | 15 | O3 or O4 |
| | | 90 | 8 | O3 or O4 | 15 | O3 or O4 |
| HFRT009 | J3-30D-03 | 0 | 73 to 75 | O3 or O4 | 75 | O3 or O4 |
| | | 180 | 83 | O3 or O4 | 75 | O3 or O4 |
| | J3-30D-04 | -90 | 4 | O3 or O4 | 15 | O3 or O4 |
| | | 0 | 96 to 99 | O1 or O2 | 105 | O1 or O2 |
| | | 180 | 102 to 103 | O1 or O2 | 105 | O1 or O2 |
| HFRT011 | J3-001-06 | 135 | 45 | O3 or O4 | 45 | O3 or O4 |
| | | -135 | 130 | O1 or O2 | 135 | O1 or O2 |
| HFRT012 | J3-001-05 | -60 | 56 | O3 or O4 | 45 | O3 or O4 |
| | J3-001-06 | -135 | 132 | O1 or O2 | 135 | O1 or O2 |
| HFRT013 | J3-001-06 | 30 | 135 | O1 or O2 | 135 | O1 or O2 |
| | | -135 | 128 | O1 or O2 | 135 | O1 or O2 |
| HFHT005 | J3-30D-05 | -45 | 70 | ?? | ?? | ?? |
| | | 0 | 79 | ?? | ?? | ?? |
| | | 0 | 97 | ?? | ?? | ?? |
| | | 30 | 104 | ?? | ?? | ?? |

# 6 Conclusions

A companion numerical submodeling technique for capturing the contact traction and near-surface stress behavior for the experimental contact has been developed. The devised submodel analysis was used to calculate surface stresses of the FCC single crystal for a range of representative experimental loading conditions. Comparison of the surface stresses to the observed experimental cracking behavior resulted in the following conclusions and observations:

- Material orientation can significantly affect the contact stresses.
- Knowledge of the resolved shear stress and normal stress magnitudes associated with the four octahedral and cube slip planes can aid in predicting where cracking will occur.
- Knowledge of the resolved shear stress and normal stress behavior for each of the four FCC single crystal octahedral planes and three cubic planes can aid the prediction of crystallographic crack orientation.
- A vast majority of experimentally observed crystallographic cracking at room temperature seems to occur on one of the four FCC single crystal octahedral planes.

Although the conclusions support the use of the resolved shear stresses and normal stresses in capturing the qualitative behavior of fretting in SCN materials, better knowledge of the actual coefficient of friction and increased mesh resolution near the edge-of-contact and stick/slip boundary of the contact are needed before quantitative comparisons can be made. Future experimental work could include performing a set of friction tests capable of capturing the room temperature and elevated temperature friction behavior for the contact investigated. Other experimental work is currently underway to characterize the fretting fatigue performance of the SCN material at an elevated temperature of $650^oC$. The material orientations for the elevated temperature test specimens need to be determined by an appropriate technique in order to relate observed cracking behavior to the corresponding crystal planes. Future modeling work could include investigating the effect of plasticity with better knowledge of the SCN material behavior. Using a sufficiently powerful computing platform to achieve an adequate mesh resolution at the edge-of-contact and stick/slip interface would also allow estimation of stresses at observed crack locations. With knowledge of these stresses and the crack geometry as obtained from a scanning electron microscope investigation of a fretted specimen subjected to a break-open test, an estimate for a fretting crack threshold intensity factor could then be calculated. Finally, the results showed that the resolved shear stresses and normal stresses for each crystal plane provided insight as to where and at what orientation cracking would occur. This suggests the development of a damage parameter that includes contributions from both resolved shear stresses and normal stresses for each crystal plane.

## References

[1] H. Murthy, G. Harish, T. N. Farris, Efficient modeling of fretting of blade/disk contacts including load history effects, Journal of Tribology (2004) in press.

[2] C. Ruiz, P. H. B. Boddington, K. C. Chen, An investigation of fatigue and fretting in a dovetail joint, Experimental Mechanics 126 (1984) 56–64.

[3] J. M. Dobromirski, Variables of fretting process: Are there 50 of them?, in: M. H. Attia, R. B. Waterhouse (Eds.), Standardization of Fretting Fatigue: Test Methods and Equipment, ASTM STP 1159, American Society of Testing and Materials, Philadelphia, PA, 1992, pp. 69–84.

[4] J. F. Matlik, High-temperature, high-frequency fretting fatigue of a single crystal nickel alloy, Ph.D. thesis, Purdue University, School of Aeronautics and Astronautics, 315 North Grant Street, West Lafayette, IN 47907-2023 (December 2004).

[5] J. Matlik, T. Farris, F. Haake, High-frequency, high-temperature fretting, Wear ??? (2005) ???

[6] R. B. Waterhouse, Fretting fatigue, International Materials Reviews 37 (1992) 77–96.

[7] M. P. Szolwinski, T. N. Farris, Mechanics of fretting fatigue crack formation, Wear 198 (1996) 193–107.

[8] D. A. Hills, D. Nowell, Mechanics of Fretting Fatigue, Kluwer Academic Publishers, Netherlands, 1994.

[9] T. N. Farris, H. Murthy, J. F. Matlik, Fretting fatigue, in: R. O. Ritchie, Y. Murakami (Eds.), Comprehensive Structural Integrity: Fracture of Materials from Nano to Macro, Vol. 4, Elsevier Science, 2003.

[10] N. G. Cormier, B. S. Smallwood, G. B. Sinclair, G. Meda, Aggressive submodelling of stress concentrations, International Journal for Numerical Methods in Engineering 46 (1999) 889–909.

[11] G. B. Sinclair, N. G. Cormier, J. H. Griffin, G. Meda, Contact stresses in dovetail attachments: Finite element modeling, Journal of Engineering for Gas Turbines and Power 124 (2002) 182–189.

[12] J. R. Beisheim, G. B. Sinclair, On the three-dimensional finite element analysis of dovetail attachments, Journal of Turbomachinery 125 (2003) 372–379.

[13] D. A. Hills, D. Nowell, A. Sackfield, Mechanics of Elastic Contacts, Butterworth-Heinemann, Oxford, Great Britain, 1993.

[14] R. L. Munisamy, D. A. Hills, D. Nowell, Static axisymmetric hertzian contacts subject to shearing forces, Journal of Applied Mechanics 61 (1994) 278–283.

[15] P. T. Rajeev, T. N. Farris, Numerical analysis of fretting contacts of dissimilar isotropic and anisotropic materials, Journal of Strain Analysis for Engineering Design 37 (6) (2002) 503–518.

[16] D. Stouffer, L. Dame, Inelastic Deformation of Metals: Models, Mechanical Properties, and Metallurgy, John Wiley & Sons, 1996.

[17] J. Telesman, L. Ghosn, The unusual near threshold fcg behavior of a single crystal superalloy and the resolved shear stress as the crack driving force, Engineering Fracture Mechanics 34 (5/6) (1989) 1183–1196.

[18] G. R. Swanson, N. K. Arakere, Effect of crystal orientation on analysis of single-crystal, nickel-based turbine blade superalloys, Tech. Rep. NASA/TP-2000-210074, National Aeronautics and Space Administration (NASA), Marshall Space Flight Center (MSFC), Alabama (February 2000).

[19] D. DeLuca, C. Annis, Fatigue in single crystal nickel superalloys, Office of Naval Research, Department of the Navy FR-23800.